Journal of Zhejiang University-SCIENCE A 2026 27(10):1138-1152
www.jzus.zju.edu.cn; www.springer.com/journal/11582
E-mail: jzus_a@zju.edu.cn

Research Article
https://doi.org/10.1631/jzus.A2600298

Check for updates

Hybrid integration of flexible temperature and humidity sensors with crosstalk decoupling for wearable physiological monitoring

Mengran LIU[1], Ziming LI[1], Yingying DAI[2], Chongjie JIANG[2], Junwen HUANG[2], Zhenghong LUO[2], Jinhui ZHANG[2], Wei ZHOU[2], Wendi GAO[3]✉, Tao LUO[2]✉

[1]*Hubei Key Laboratory of Modern Manufacturing Quality Engineering, School of Mechanical Engineering, Hubei University of Technology, Wuhan 430068, China*
[2]*School of Intelligent Manufacturing (Pen-Tung Sah Institute of Micro-Nano Science and Technology), Xiamen University, Xiamen 361102, China*
[3]*Department of Gastroenterology, Second Affiliated Hospital of Xi'an Jiaotong University; School of Instrument Science and Technology, the State Key Laboratory for Manufacturing Systems Engineering, the State Industry-Education Integration Center for Medical Innovations, the International Joint Laboratory for Micro/Nano Manufacturing and Measurement Technologies, Xi'an Jiaotong University, Xi'an 710049, China*

Abstract: Accurate, synchronous monitoring of respiratory and cutaneous temperature and humidity is essential for assessing pulmonary function and exercise-induced metabolic status. However, miniaturized flexible sensors often suffer from temperature-humidity crosstalk, which degrades measurement reliability. Here, we present a flexible temperature-humidity sensor that achieves crosstalk decoupling through hybrid integration of thermoelectric temperature sensing and capacitive humidity sensing, combined with algorithmic compensation. A 3D interconnected copper-constantan thin-film thermocouple is fabricated on a polyimide substrate for temperature measurement. On the same substrate, a capacitive humidity sensor is constructed using laser-induced graphene interdigital electrodes and a graphene oxide sensing layer. Leveraging the intrinsic immunity between ionic and electronic conduction mechanisms, together with compensation algorithms, real-time decoupled sensing is achieved. The device exhibits an average humidity sensitivity of 31 pF/%RH (relative humidity) and a temperature sensitivity of 29.88 μV/°C, with fast response and recovery. A flexible printed circuit-based acquisition module with wireless transmission is further developed for wearable operation. Demonstrations in respiration monitoring and exercise metabolic assessment scenarios confirm the reliable capture of temperature-humidity dynamics, highlighting the potential of the proposed sensor for wearable healthcare applications.

Key words: Flexible sensors; Temperature-humidity monitoring; Crosstalk decoupling; Epidermal electronics; Physiological monitoring

1 Introduction

Wearable physiological monitoring devices hold substantial promise for personalized health management and early disease prediction (Gao et al., 2016; Bandodkar et al., 2019; Kim et al., 2019). Synchronous monitoring of respiratory and cutaneous microenvironmental temperature and humidity provides critical physiological insights (Baker et al., 2020; Yin et al., 2024; Zhou et al., 2024). Minute fluctuations in respiratory temperature provide useful information for respiratory monitoring, while epidermal temperature-humidity dynamics reflect thermoregulatory capacity and metabolic status (Nyein et al., 2021; Yin et al., 2024). Concurrent assessment of respiratory patterns and cutaneous temperature-humidity variations therefore enables effective discrimination of exercise states and early detection of disease risk (Baker et al., 2020; Yin et al., 2024; Zhou et al., 2024). Beyond multimodal signal acquisition, learning-based approaches have also been introduced into soft wearable systems to suppress signal artifacts, extract complex physiological information, and improve user-independent adaptation, further highlighting the importance of reliable multimodal sensing as the basis for intelligent physiological monitoring (Kim et al., 2020, 2023, 2026; Park et al., 2026).

✉ Tao LUO, luotao@xmu.edu.cn
Wendi GAO, wendi_gao@mail.xjtu.edu.cn
Tao LUO, https://orcid.org/0000-0002-4861-3397
Wendi GAO, https://orcid.org/0000-0001-5243-6007

Received May 7, 2026; Revision accepted Sept. 11, 2026;
Crosschecked Sept. 21, 2026; Online first Oct. 31, 2026

© Zhejiang University Press 2026

Contemporary flexible humidity sensors mainly rely on piezoresistive, capacitive, and triboelectric transduction mechanisms (Kuzubasoglu, 2022). Among them, capacitive sensors offer superior linearity, high sensitivity, and low power consumption, making them particularly suitable for continuous respiratory monitoring (Yin et al., 2024). In recent years, laser-induced graphene (LIG) technology has emerged as a cost-effective and patternable approach for constructing flexible capacitive sensors (Lan et al., 2020; Zhu et al., 2020; Fei et al., 2023). Its direct laser patterning ability and tunable porous structure have enabled diverse device configurations, including mechanically robust freestanding electrodes, biodegradable sensing platforms, and flexible sensing and energy devices (Jung et al., 2022; Le et al., 2022; Choi and Ko, 2026; Choi et al., 2026). Porous LIG electrodes can be directly fabricated on polyimide (PI) substrates by laser scribing, and integration with graphene oxide (GO) sensing layers enables high-sensitivity humidity detection, with sensitivities reaching several thousand pF/%RH (relative humidity) (Lan et al., 2020; Zhu et al., 2020; Fei et al., 2023). This response originates from dielectric constant modulation caused by water intercalation within GO layers and from changes in ionic conductivity due to proton hopping mediated by hydrophilic functional groups (Bi et al., 2013; Ghosh et al., 2015). However, the humidity response of GO is intrinsically coupled with temperature (Wu et al., 2019). Elevated temperatures accelerate proton mobility and disturb adsorption equilibrium, producing thermal drift in humidity signals (Wu et al., 2019). Conversely, humidity variations also interfere with conventional flexible resistive temperature sensors, especially those sensors using carbon-based nanomaterials as temperature-sensitive materials (Rohilla et al., 2025). These devices rely on interfacial charge transport and are highly sensitive to water adsorption, electrochemical effects, and substrate swelling, resulting in severe signal coupling that degrades the accuracy of temperature measurements under humidity fluctuating environments.

Strategies for mitigating crosstalk in soft multimodal sensors span multiple levels, including sensing-element-level interference suppression, structural or array-level isolation, spatiotemporal separation, and algorithm- or data-driven signal compensation (Mu et al., 2024; Wu et al., 2026; Yuan et al., 2026). Spatial isolation can partially reduce interference. For example, tri-modal sensing of temperature, humidity, and pressure based on 3D vertical lamination has achieved cross-sensitivity below 0.6% (Mu et al., 2024). However, such approaches may increase device thickness and compromise wearing comfort, while thermal-conduction-induced drift can persist during long-term operation (Wu et al., 2026). This limitation becomes particularly relevant for long-term wearable physiological monitoring, in which temperature and humidity fluctuate simultaneously (Shen et al., 2024). System-level developments have further incorporated local signal processing and highly integrated stretchable platforms to enhance multimodal information processing and autonomous operation (Liu et al., 2024; Ren et al., 2025). Algorithmic compensation can correct signal drift to some extent; however, bidirectional coupling between temperature and humidity often necessitates relatively complex compensation models with limited generalizability (Jia et al., 2025), posing a major challenge to high-precision multimodal sensing in miniaturized and highly integrated flexible devices. Therefore, reducing intrinsic coupling between sensing channels prior to algorithmic correction is particularly desirable, as it can simplify subsequent signal decoupling while preserving compact device integration for wearable physiological monitoring (Yang et al., 2022; Wu et al., 2026).

To address these challenges, this work proposes a hybrid integration strategy that combines thermoelectric temperature sensing and capacitive humidity sensing on a single PI substrate. Temperature sensing is based on the Seebeck effect of a copper-constantan thermocouple, in which a temperature difference between the hot and cold junctions generates a thermoelectric voltage. Humidity sensing relies on proton transport within the GO interlayers, where adsorbed water molecules form hydrogen-bonded networks that facilitate ionic conduction, leading to measurable variations in capacitance. Owing to these distinct transduction mechanisms, temperature variations influence the capacitance of the humidity sensor, whereas humidity exerts a negligible effect on the thermocouple output. This unidirectional and predictable crosstalk provides a favorable basis for accurate signal decoupling. Building on this hybrid sensing architecture, a simple second-order polynomial regression model is developed to compensate for the temperature-induced drift in the humidity response. Consequently, the integrated bimodal sensor enables accurate and effectively

decoupled temperature and humidity measurements, achieving a temperature sensitivity of 29.88 μV/℃ and a humidity sensitivity of 31 pF/%RH. Furthermore, when integrated with a custom-designed flexible printed circuit (FPC)-based signal readout and acquisition system with wireless data transmission, the platform demonstrates practical capabilities for wearable monitoring of respiration, coughing, and dorsal-hand sweating.

2 Materials and methods

2.1 Materials

The GO dispersion with an initial concentration of 5 mg/mL (Xianfeng Nano, China) was diluted with deionized water to a working concentration of 4.5 mg/mL. Customized FPC substrates (JLCPCB, China) consisting of 110 μm thick copper-clad films were used for the fabrication of the integrated flexible sensor. A constantan target with a purity of 99.99% (Nanjing Mingchang New Materials, China) was used for deposition of the negative thermocouple electrodes. All aqueous solutions were prepared using deionized water.

2.2 Fabrication of the flexible sensor

As shown in Fig. S1 of the electronic supplementary materials (ESM), LIG interdigital electrodes (IDEs) were initially fabricated on the FPC substrate using a 355 nm ultraviolet (UV) laser (SINO-GALVO WE-UV-10W, China) with a focal length of 22.5 cm, pulse width of 10 μs, scanning speed of 15 mm/s, and frequency of 24 kHz. The resulting IDEs comprised nine finger pairs, each with a finger length of 1.5 mm, finger width of approximately 200 μm, and inter-finger spacing of approximately 150 μm. Subsequently, oxygen plasma treatment was applied to the exposed IDE region to enhance hydrophilicity and remove contaminants. A 5 μL GO dispersion with a concentration of 4.5 mg/mL was drop-cast onto the IDEs and annealed at 60 ℃ for 30 min. For the thermocouple junction, a 400 nm thick constantan film was deposited on the opposite side of the FPC substrate by magnetron sputtering and electrically connected to copper vias, forming 3D interconnected copper-constantan thermocouple junctions. Finally, the constantan layer was encapsulated with insulating ink, while the LIG IDEs remained exposed for humidity sensing.

2.3 Material characterization and sensor test

The microstructural morphologies of the LIG IDEs and the GO thin film were characterized by scanning electron microscopy (SEM) (Zeiss Sigma 360, Germany). Raman spectroscopy (Zhongyan Huanke DEEP-INRS-II, China) was employed to investigate the molecular structure of these materials. X-ray photoelectron spectroscopy (Thermo Scientific K-Alpha, USA) was used to analyze the surface elemental composition and chemical states.

The temperature-sensing characteristics were measured in a temperature-controlled water bath, and the transient response was evaluated using instantaneous laser irradiation-induced heating. Humidity-sensing performance was assessed in a homemade temperature-humidity chamber (Fig. S2 of the ESM). Two air pumps directed gas flows through desiccant and humidifier bottles, respectively, and the combined stream entered a mixing chamber. The chamber temperature was regulated using flexible PI heating films, while a commercial reference temperature-humidity sensor was placed adjacent to the proposed flexible sensor to enable accurate calibration and performance characterization.

2.4 Design of the FPC-based sensor readout and acquisition system

To enable real-time signal acquisition of the sensor, a portable FPC-based monitoring system was developed. The core of the system consists of an AD5941 impedance analysis chip, an HX711 voltage acquisition chip, and an ESP32-C3 Bluetooth microcontroller. AD5941 generates a high-frequency alternating current (AC) excitation to measure the complex capacitance between LIG interdigital electrodes for humidity sensing. The HX711 24-bit analog-to-digital converter (ADC) acquires the thermocouple voltage, while AD5941 additionally monitors a cold-junction PT1000 resistor for cold-end compensation of the thermocouple. A high-speed multiplexing scheme enables quasi-synchronous acquisition of temperature and humidity signals. A decoupling compensation algorithm is embedded in the ESP32 firmware, dynamically correcting humidity capacitance measurements using real-time temperature values obtained by the thermocouple. The processed data are wirelessly transmitted via Bluetooth. The circuit is powered by a rechargeable lithium-ion battery with a capacity of 1100 mAh and a nominal voltage of 3.7 V.

3 Results and discussion

3.1 Design of the integrated bimodal flexible temperature and humidity sensor system

To suppress crosstalk between temperature and humidity signals, an integrated flexible temperature-humidity sensor based on a vertically stacked heterogeneous architecture was developed, together with a data acquisition FPC (Fig. 1a). The sensor conformably attaches to the dorsal hand for physiological monitoring, while the FPC is secured around the wrist, ensuring system compactness and wearing comfort. The integrated bimodal sensor adopts a six-layer vertical stacking structure (Fig. 1b). The top layer is a patterned solder mask that exposes only the humidity-sensitive region. The second layer consists of a GO humidity-sensitive film deposited on LIG IDEs. The third layer comprises the LIG interdigital electrodes and copper interconnects, where copper traces are electrically connected to the constantan layer through vias. The fourth layer is the PI substrate, which serves as the supporting and isolation layer. The fifth layer is the

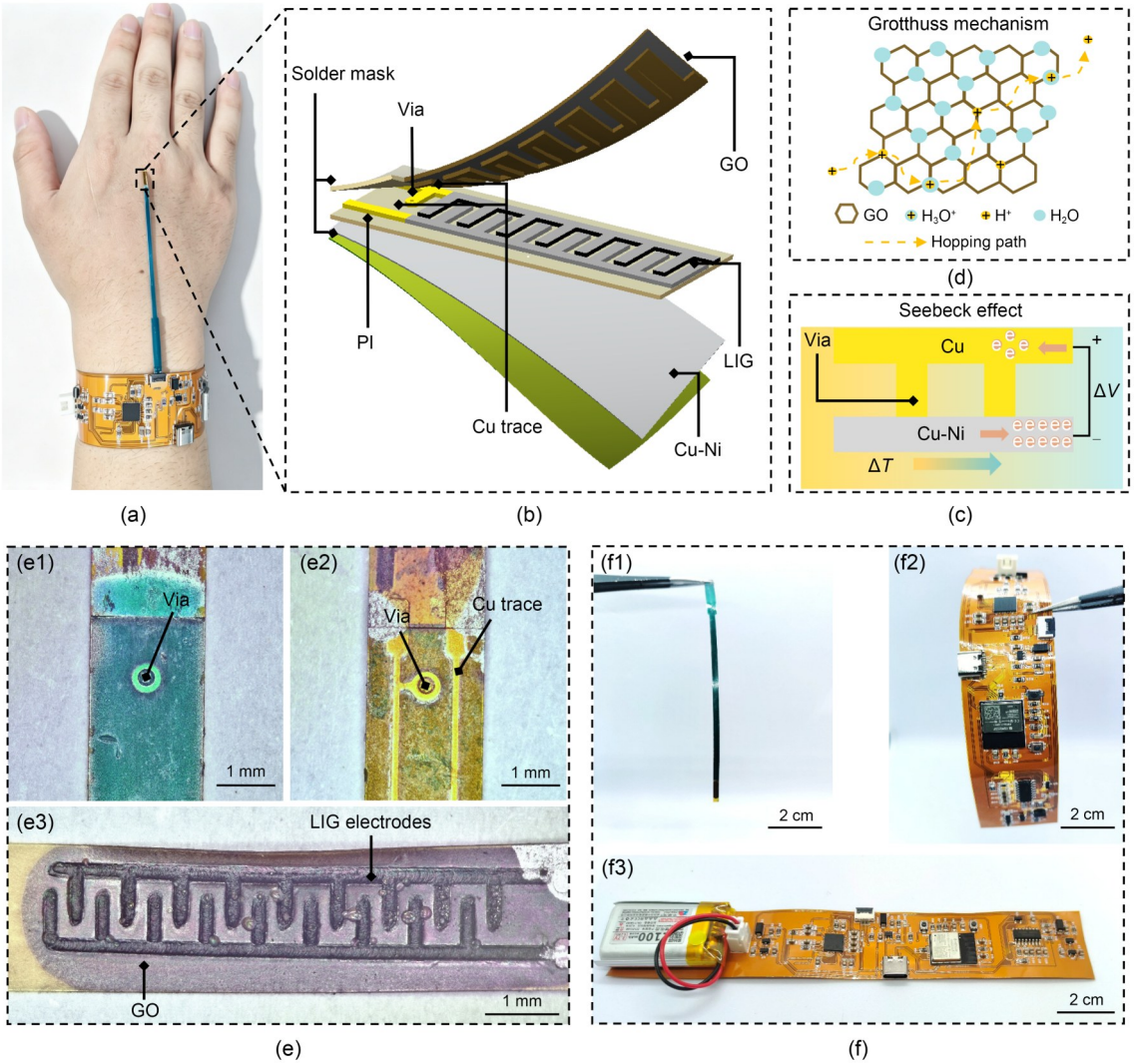

Fig. 1 Structure and sensing mechanisms of the integrated flexible sensor: (a) photograph of the integrated bimodal flexible sensor attached to the dorsal hand, with the FPC-based data acquisition system worn on the wrist; (b) schematic of the six-layer vertically stacked architecture of the flexible sensor; (c) temperature-sensing principle based on the Seebeck effect of a copper-constantan thermocouple; (d) humidity-sensing principle based on the Grotthuss proton-hopping mechanism in GO; (e1, e2) optical micrographs of the thermocouple junction/via and Cu trace; (e3) LIG interdigital electrodes coated with GO; (f1–f3) photographs demonstrating device flexibility and integration with the FPC board acquisition platform

constantan film, where copper-constantan thermocouple junctions are formed, and the bottommost layer is a full-coverage solder mask providing electrical insulation and mechanical protection.

The transduction mechanism of bimodal sensing relies on fundamentally different ionic and electronic conduction processes. The temperature-sensing unit is based on the Seebeck effect in copper-constantan thin-film thermocouples (Fig. 1c), whereas the humidity-sensing unit operates through Grotthuss proton hopping within GO interlayers (Fig. 1d). This hybrid integration intrinsically suppresses crosstalk at the mechanism level. The thermocouple junction adopts a 3D interconnected structure (Figs. 1e1 and 1e2). As shown in Fig. 1e3, the LIG IDEs feature a nine-pair finger configuration and are uniformly coated with the GO film. Both the data acquisition FPC and the bimodal sensor exhibit excellent mechanical flexibility for wearable applications, as demonstrated in Fig. 1f.

3.2 Characterizations of the sensor materials

To elucidate the capacitive response mechanism of the humidity sensor at the microscopic level, comprehensive characterizations of the humidity-sensing materials were performed. Cross-sectional optical micrographs (Fig. 2a) confirm that, in this vertical heterostructure, multiple LIG layers are induced in an expanded state, forming 3D electrodes to substantially increase the effective capacitive response area. The GO film maintains intimate contact with the LIG without discernible gaps, ensuring signal stability. As shown in Fig. 2b, the UV laser-scribed LIG electrodes exhibit a 3D porous structure, which provides abundant 3D transport channels for water-molecule adsorption. In contrast, the GO film exhibits a relatively smooth morphology with numerous interlayer voids, facilitating water infiltration.

Raman spectroscopy further elucidates the crystallographic characteristics of the materials (Fig. 2c). Both LIG and GO exhibit prominent D and G peaks at approximately 1350 and 1580 cm^{-1}, respectively. LIG additionally shows a distinct 2D peak at about 2700 cm^{-1} ($I_{2D}/I_G \approx 0.27$), characteristic of graphitic structures, whereas GO presents an attenuated 2D band ($I_{2D}/I_G \approx 0.14$), consistent with its oxidized structure. The LIG/GO composite exhibits a ratio of 0.26, close to that of LIG. High-resolution C 1s deconvolution from X-ray photoelectron spectroscopy of GO (Fig. 2d) reveals substantial amounts of hydrophilic functional groups, including C–O(H), C=O, and COOH.

3.3 Sensor performance tests

As shown in Fig. 3a, the thermocouple-based temperature sensor was tested over a temperature difference ranging from 0 to 27 °C. Linear fitting yields a correlation coefficient of R^2=0.997, with a sensitivity of approximately 29.88 μV/°C. To investigate the sample-to-sample variation of the temperature sensor, three sensors from the same batch were tested under identical conditions, and the inter-sensor variation in sensitivity was evaluated based on their calibration results (Fig. 3b). The temperature sensitivity was determined to be (30.71±0.66) μV/°C, with the error bars representing the standard deviation (SD). The hot junction was rapidly heated by pulsed laser irradiation to evaluate the response and recovery times of the temperature sensor, showing a response time of approximately 5.38 s and a recovery time of approximately 5.39 s, as presented in Fig. 3c. To assess the stability of the temperature sensor under cyclic heating, laser irradiation with 2.5 s switching intervals was applied (Fig. 3d), and the device exhibited highly consistent output under repeated cyclic laser heating. To evaluate its mechanical robustness, we tested the sensing performance under five bending radii of 5.0, 7.5, 10.0, 12.5, and 15.0 mm. Compared with the unbent baseline, the thermoelectric voltage changes of the sensor under a temperature variation of 10 °C remained stable at approximately 0.31 mV across the different bending conditions. This value is only slightly lower than the response of 0.32 mV measured in the unbent state, corresponding to a relative error of approximately 3.1%, as shown in Fig. 3e. To evaluate the long-term stability of the sensor, the temperature responses were continuously monitored over a period of 7 d. As shown in Fig. 3f, the temperature output remained stable throughout the entire testing period, with mean responses of (0.169±0.016), (0.432±0.005), (0.800±0.005), and (1.168±0.010) mV at temperature differences (ΔT) of 2, 10, 20, and 28 °C, respectively.

Performance characterization of the LIG/GO-based flexible humidity sensor was conducted in sealed environments with varying humidity levels. The sensitivity of the humidity sensor depends on multiple parameters. First, the influence of different GO concentrations on the sensitivity and dynamic response of the sensor was

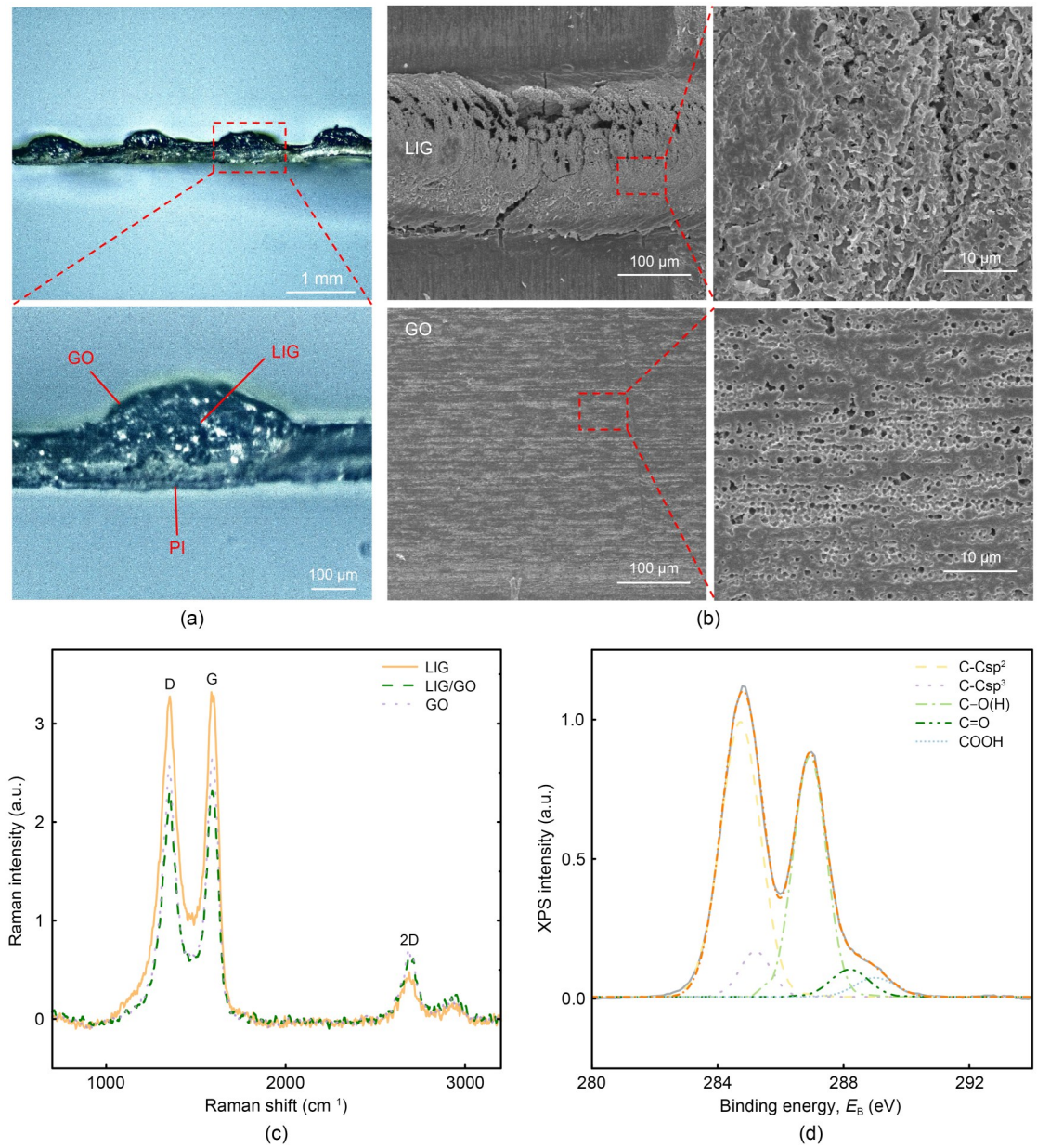

Fig. 2 Microstructural and compositional characterization of the sensing materials: (a) cross-sectional optical micrograph showing intimate contact between LIG IDEs and GO film; (b) surface SEM images of the LIG IDE and GO film at different magnifications; (c) Raman spectra of LIG, GO, and LIG/GO composite materials; (d) high-resolution C 1s X-ray photoelectron spectroscopy (XPS) spectrum of the GO film

evaluated at a fixed frequency of 1 kHz, as shown in Fig. 3g. Subsequently, at the optimized GO concentration of 4.5 mg/mL, the sensor's response characteristics were investigated at different test frequencies (Fig. 3h). The experimental results demonstrate that, with a GO concentration of 4.5 mg/mL and an operating frequency of 1 kHz, the sensor exhibits optimal overall performance in terms of sensitivity and linearity, achieving a sensitivity of 31 pF/%RH. To evaluate the sample-to-sample variation of the humidity sensor, three sensors from the same batch were tested under identical conditions (Fig. 3i). The humidity sensitivity was determined to be (31.00±2.73) pF/%RH, with the error bars representing the SD. The coefficient of variation of the humidity sensitivity was approximately 8.8%, compared with approximately 2.1% for the temperature sensitivity, indicating relatively larger sample-to-sample variation in the humidity channel. For the

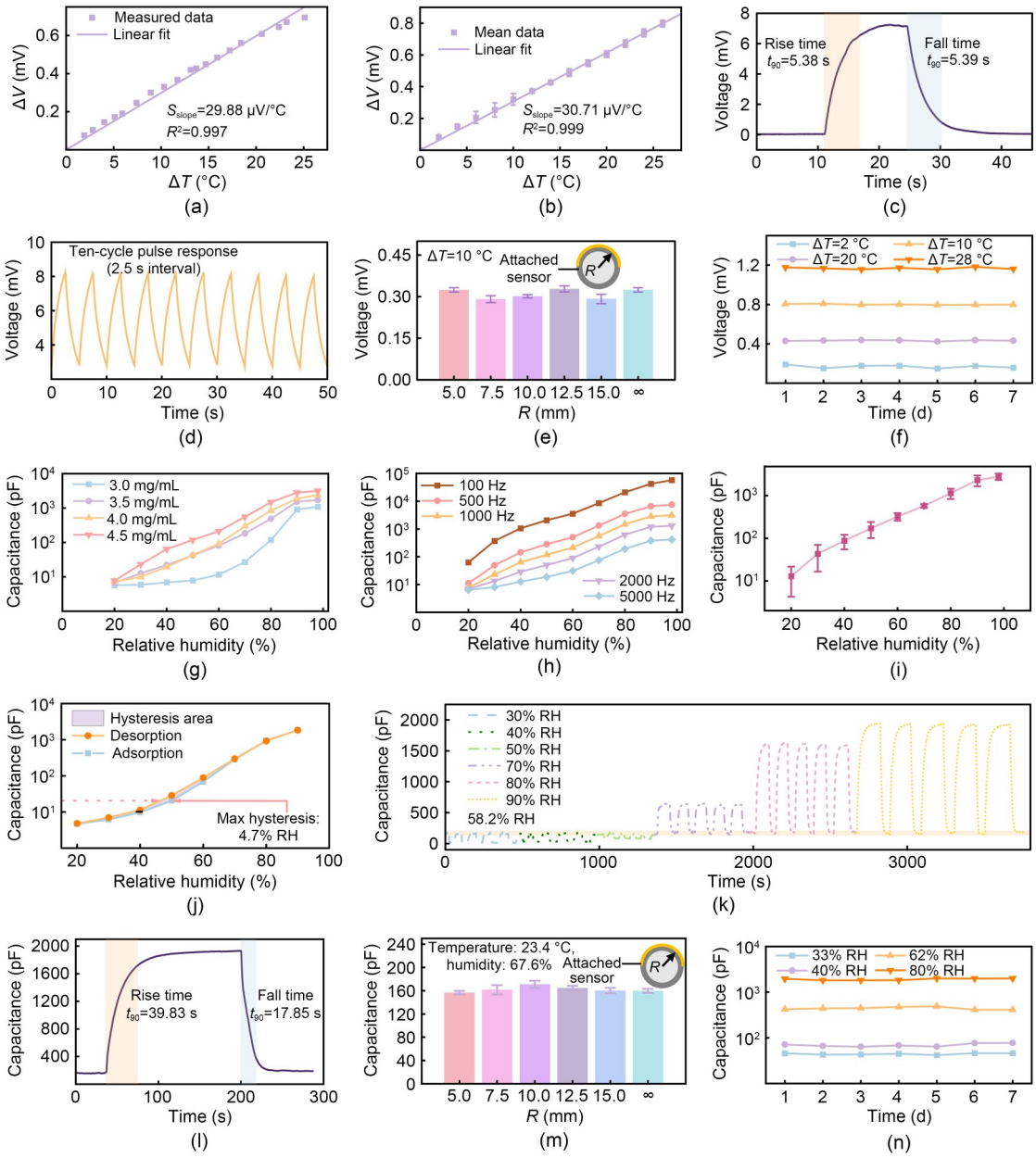

Fig. 3 Performance evaluation of the temperature and humidity sensing units: (a) calibration curve and linear fit of the thermoelectric voltage (Δ*V*) versus temperature difference (Δ*T*) for a representative copper-constantan thermocouple, where S_{slope} denotes the sensitivity determined from the linear-fit slope; (b) sample-to-sample reproducibility of the temperature sensor, showing the mean thermoelectric response and SD obtained from three independently fabricated sensors (*n*=3); (c) transient response and recovery characteristics of the temperature sensor under pulsed laser heating, where t_{90} denotes the 90% response/recovery time; (d) cyclic response of the temperature sensor under ten consecutive laser-heating cycles with a 2.5 s interval; (e) thermoelectric voltage stability of the temperature sensor under different bending radii at Δ*T*=10 °C, where *R* denotes the bending radius; (f) long-term voltage-response stability of the temperature sensor over a 7-d period under different temperature differences; (g) capacitive response of the humidity sensor prepared with different GO concentrations at 1 kHz; (h) capacitive response of the humidity sensor at different operating frequencies using the optimized GO concentration of 4.5 mg/mL; (i) sample-to-sample reproducibility of the capacitance response to relative humidity obtained from three independently fabricated humidity sensors (*n*=3); (j) adsorption-desorption hysteresis of the humidity sensor over 20%–90% RH; (k) capacitance response of the humidity sensor during repeated multilevel relative-humidity cycling; (l) dynamic response and recovery of the humidity sensor to a step change from 58.2% RH to 90% RH; (m) capacitive output stability of the humidity sensor under different bending radii at 23.4 °C and 67.6% RH; (n) long-term capacitive-response stability of the humidity sensor over a 7-d period at 33%, 40%, 62%, and 80% RH

temperature sensors, some sample-to-sample variation was also observed in the absolute thermoelectric output of the temperature sensors at low temperature differences. For example, at a temperature difference of 2 ℃, the voltage outputs of the three sensors were 76.10, 73.98, and 97.63 μV, respectively. In contrast, a larger sample-to-sample variation was observed in the absolute baseline capacitance of the humidity sensors. At 20% RH, for example, the capacitances of the three sensors were 22.9, 7.8, and 8.1 pF, respectively. The measured absolute capacitance contains contributions from both the sensing element and parasitic capacitance associated with the external electrical connections and measurement configuration. Variations in these parasitic contributions may introduce offsets in the absolute capacitance, whereas the humidity sensitivity is determined from the capacitance change with RH under a fixed measurement configuration. Consequently, the humidity sensitivity exhibited substantially smaller sample-to-sample variation than the absolute baseline capacitance. The hysteresis of the optimized humidity sensor was also evaluated. As shown in Fig. 3j, during 20%–90% RH humidity cycling, the maximum hysteresis is 4.7% RH, indicating low humidity hysteresis. The humidity sensor also demonstrates good consistency over six consecutive response cycles in the high-humidity regime (>60% RH), as shown in Fig. 3k. In the low-humidity regime (<40% RH), relatively larger fluctuations are observed because the reduced capacitive baseline results in a lower signal-to-noise ratio and greater susceptibility to noise. The baseline drift and cycle-to-cycle variation may also arise from incomplete desorption of residual interlayer water, slow re-equilibration of hydrophilic functional groups, and slight charge trapping. In addition, the maximum hysteresis of 4.7% RH over the 20%–90% RH range is primarily attributed to the asymmetric intercalation and de-intercalation of water molecules within the GO interlayers. Fig. 3l displays the dynamic response from 58.2% RH to 90% RH, with a response time of approximately 39.83 s and a recovery time of approximately 17.85 s. It should also be noted that the response/recovery time (39.83/17.85 s) and maximum hysteresis (4.7% RH) reported in Figs. 3l and 3j were obtained using a representative sensor. The reported R^2 values were calculated from calibration data obtained at distinct temperature or relative-humidity levels, rather than from repeated measurements at a single condition. For humidity sensing, at a temperature of 23.4 ℃ and a relative humidity of 67.6%, the sensor capacitance exhibited a maximum variation of ±5.43 pF under bending, corresponding to approximately 3.3% of the baseline capacitance of 162.89 pF, as shown in Fig. 3m. These results demonstrate that both the temperature and humidity sensing functions remain stable under moderate bending deformation, confirming the suitability of the sensor for conformal wearable applications. To evaluate the long-term stability of the humidity sensor, its capacitive response was monitored over a period of 7 d. As shown in Fig. 3n, the humidity sensor exhibited stable responses over the 7-d period, with mean capacitance values of (44.43±1.72) pF at 33% RH, (69.57±5.57) pF at 40% RH, (441.66±30.52) pF at 62% RH, and (1915.75±89.08) pF at 80% RH.

3.4 Crosstalk decoupling of the integrated bimodal flexible sensor

To achieve crosstalk decoupling in the integrated bimodal flexible sensor, a strategy combining intrinsic crosstalk suppression and algorithmic compensation was employed. Intrinsic crosstalk suppression is realized by the hybrid integration of thermoelectric temperature sensing with capacitive humidity sensing. For algorithmic compensation, the temperature sensor was first calibrated under 30% RH and 100% RH environments (Fig. 4a). The results show that humidity exerts no significant influence on temperature calibration. The integrated bimodal flexible sensor was then placed in an environment with a constant hot-to-cold temperature difference of 13 ℃, and the voltage of the thermocouple was recorded in 10% RH increments from 20% RH to 90% RH (Fig. 4b). No discernible drift was observed. The negligible susceptibility of the temperature channel to humidity can be attributed to two factors. First, the Seebeck transduction mechanism of the copper-constantan thermocouple dictates that the generated thermoelectric voltage is determined primarily by the temperature difference between the hot and cold junctions and the intrinsic thermoelectric properties of the metallic conductors, which are largely insensitive to water adsorption under the tested conditions. Second, the thermocouple layer is encapsulated with insulating ink, thereby limiting direct moisture exposure of the copper and constantan electrodes. Consequently, the negligible humidity-induced variation

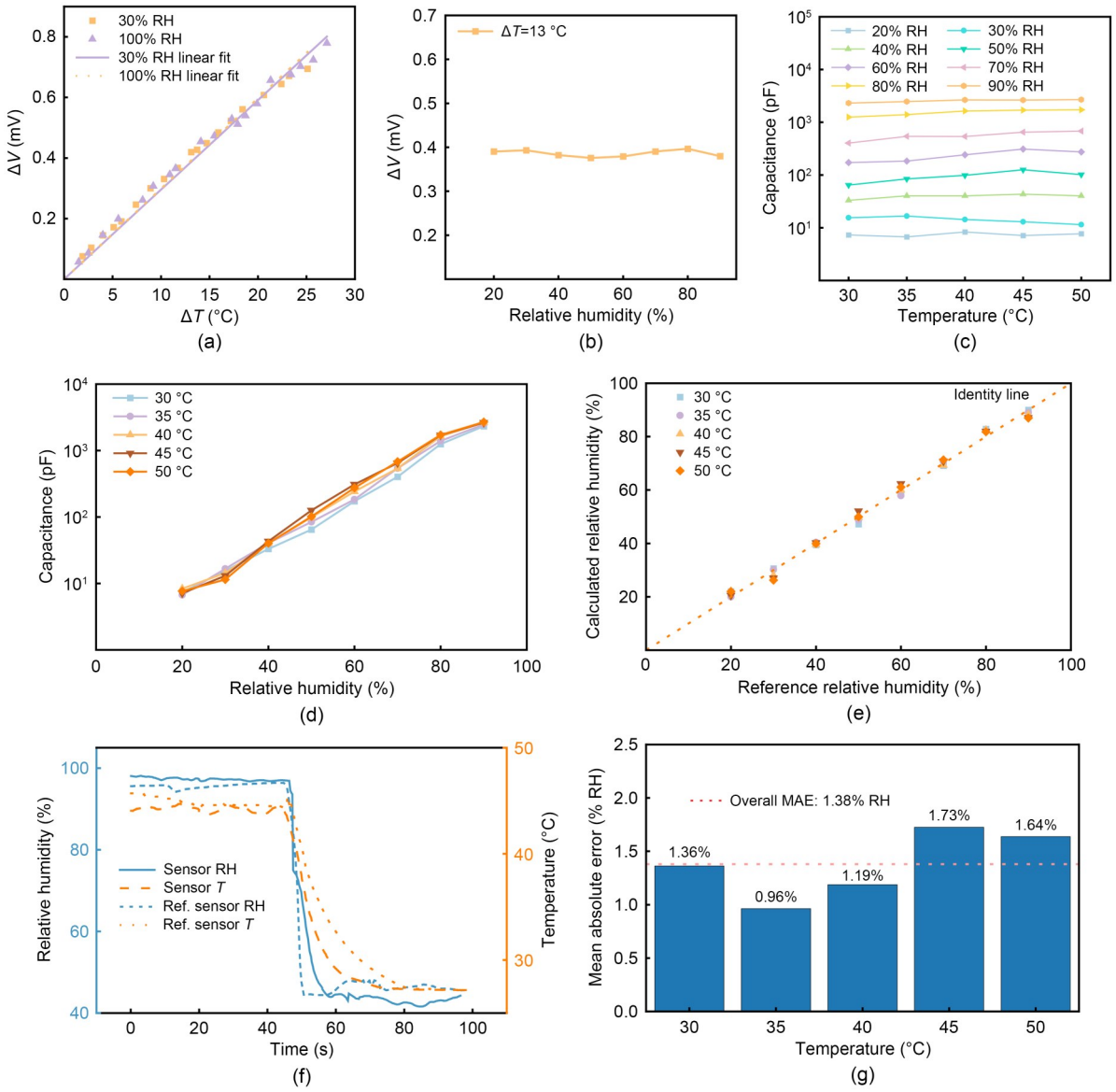

Fig. 4 Crosstalk evaluation and decoupling via a second-order polynomial model: (a) calibration of the temperature sensor under environments with distinct relative humidity levels of 30% and 100%; (b) response of the temperature sensor to a constant hot-to-cold junction temperature difference of 13 °C as the relative humidity increases from 20% to 90%; (c) responses of the humidity sensor at specific relative humidity levels as the temperature increases from 30 to 50 °C; (d) raw experimental dataset used to establish the second-order polynomial regression model; (e) comparison between the compensated humidity measurement results and the identity line; (f) dynamic decoupling performance under a simultaneous wide-range temperature-humidity transition from 44.6 °C/98% RH to 27.2 °C/43% RH, compared with a commercial reference sensor; (g) mean absolute errors (MAEs) of humidity measurements at different temperatures after algorithmic compensation

in the temperature signal observed in Figs. 4a and 4b indicates that crosstalk from the humidity channel to the temperature channel is intrinsically suppressed. Subsequently, the influence of temperature on humidity sensing was evaluated by applying five temperature levels with 5 °C increments. The results reveal that temperature induces a noticeable, positively correlated drift in the capacitance of the humidity sensor (Fig. 4c), indicating a non-negligible unidirectional crosstalk effect of temperature on humidity sensing in the integrated flexible sensor. Fig. 4d presents the humidity response characteristics at multiple temperatures. Quantitatively, when the relative humidity was varied from 20% to 90% RH at a fixed hot-to-cold

junction temperature difference of 13 °C, the thermocouple output exhibited a maximum humidity-induced variation of 20.74 μV, corresponding to an equivalent temperature variation of approximately 0.69 °C (Fig. 4b). In contrast, when the temperature was increased from 30 to 50 °C at a fixed relative humidity of 90% RH, the capacitance of the humidity sensor changed by 373.24 pF, corresponding to an equivalent humidity error of approximately 3.5% RH (Figs. 4c and 4d). Therefore, prior to algorithmic compensation, the raw integrated sensor exhibits reduced and strongly asymmetric crosstalk rather than complete decoupling, because humidity-induced interference in the temperature channel is intrinsically suppressed, whereas residual temperature-induced interference remains in the humidity channel. To decouple this crosstalk, a polynomial regression-based compensation algorithm was introduced:

$$\ln C=\beta_0+\beta_1\cdot\varphi+\beta_2\cdot T+\beta_3\cdot\varphi^2+\beta_4\cdot\varphi\cdot T+\beta_5\cdot T^2, \quad (1)$$

where C denotes the measured capacitance, φ represents RH, T indicates temperature, and β_i are coefficients determined through least-squares fitting. The quadratic terms capture the nonlinear curvature observed in Fig. 4d, while the cross-term accounts for the crosstalk effect, wherein temperature sensitivity varies with humidity level. The model achieves high fitting accuracy with R^2=0.994, and the detailed fitting coefficients and decoupling schematic diagrams are provided in Table S1 and Fig. S3 of the ESM.

Fig. 4e illustrates the compensation results after crosstalk decoupling. Using the derived compensation formula, humidity values at various temperatures were calculated, and the compensated data closely aligned with the identity line, validating the effectiveness of the decoupling algorithm. To further evaluate the decoupled sensing performance under simultaneous and wide-range temperature-humidity variations, a temperature-humidity shock experiment was conducted by rapidly changing the environment from 44.6 °C/98% RH to 27.2 °C/43% RH, corresponding to concurrent changes of more than 17 °C and 50% RH. As shown in Fig. 4f, the recovered temperature and humidity signals closely tracked the environmental transition and stabilized at the new equilibrium values without evident residual crosstalk-induced distortion. At the equilibrium plateaus before and after the transition, the recovered signals showed good agreement with those measured by a commercial reference temperature-humidity sensor (WM102 equipped with an SHT45 sensing element, Rejeee, China), with mean absolute errors (MAEs) of 1.85% RH for humidity and 0.32 °C for temperature. These results demonstrate that the proposed second-order compensation method remains effective under simultaneous, wide-range variations in both temperature and humidity. Fig. 4g presents the error statistics between the calibrated data and the reference humidity, demonstrating that the mean error at each temperature remains below 2% RH, with a overall MAE of 1.38% RH. It should be noted that the second-order polynomial model was established using calibration data acquired over the ranges of 30–50 °C and 20%–90% RH (Figs. 4c and 4d) and is primarily intended for wearable physiological and skin-microclimate monitoring under the indoor and exercise-related conditions investigated in this work. Although the simultaneous temperature-humidity step test demonstrates effective compensation during a limited excursion beyond the calibration domain (Fig. 4f), the model has not been systematically validated under arbitrary out-of-range conditions. Therefore, additional calibration and validation would be required before extending its use to substantially different environmental conditions.

3.5 Application demonstrations for wearable physiological monitoring

To evaluate the practical utility of the integrated bimodal flexible sensor system for wearable physiological monitoring, an FPC-based data acquisition platform was developed. The system consists of a flexible temperature-humidity bimodal sensor integrated with an ESP32-C3 low-power data acquisition module. The overall hardware architecture is shown in Fig. 5a. The acquisition module uses an RT9193 low-dropout regulator (LDO) to provide a stable 3.3 V power supply. An AD5941 impedance measurement chip is used to acquire the raw capacitance signal (C_{Humidity}) from the humidity sensor. It also acquires the raw resistance signal (R_{Cold}) from the PT1000 platinum resistance thermometer, which serves as the cold-junction compensation sensor for the thermocouple. An HX711 high-precision ADC is used to acquire the raw voltage signal (V_{Hot}) from the thermocouple. A detailed circuit design can be found in Fig. S4. The raw signals are processed in real time using an embedded

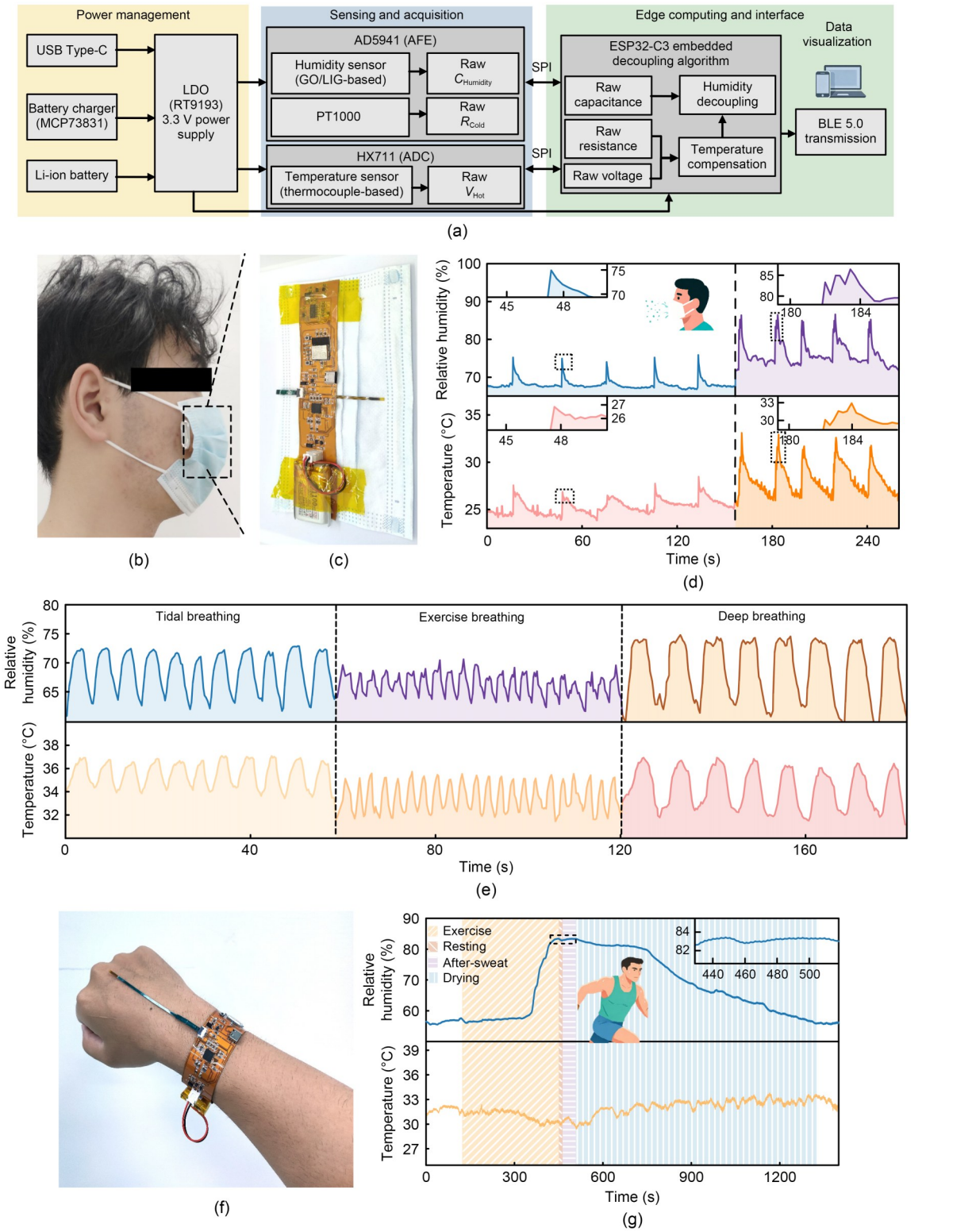

Fig. 5 Wearable physiological monitoring of respiration, coughing, and exercise: (a) hardware architecture of the acquisition system based on an ESP32-C3 microcontroller; (b and c) photographs of the sensor system attached to the inner surface of a commercial mask; (d) response of the bimodal sensor to cough events; (e) synchronized temperature-humidity waveforms during tidal breathing, exercise breathing, and deep breathing; (f) sensor system attached to the dorsal hand; (g) dynamic evolution of skin temperature and humidity during exercise monitored by the sensor system

second-order polynomial regression algorithm for temperature-humidity crosstalk decoupling. Owing to its excellent mechanical flexibility, the system can be integrated onto the inner surface of commercial masks for respiratory monitoring (Figs. 5b and 5c). It can also be configured as a wrist-worn device with the sensor attached to the dorsal hand.

The cough detection capability of the system was first evaluated, as shown in Fig. 5d. Two types of cough events were deliberately generated in separate time intervals. The first type consisted of single coughs repeated five times with an interval of approximately 30 s. The second type comprised three consecutive coughs, with each group separated by an interval of approximately 20 s. As shown in Fig. 5d, a single cough event produces a distinct unimodal spike in both the temperature and humidity channels, whereas three consecutive coughs at intervals of approximately 0.5 s generate three corresponding sub-peaks. These results confirm that the system can accurately detect cough events and resolve the underlying physiological details. Quantitatively, the temperature-humidity integral area ratio (η) was introduced as a physiological descriptor. Single coughs exhibit an integral area ratio of 0.74±0.16, while three consecutive coughs show a ratio of 0.65±0.10. This scale invariance suggests that η is an intrinsic physiological parameter of alveolar exhalation, demonstrating significantly greater robustness than conventional metrics based solely on the frequency and intensity of unimodal temperature or humidity signals. Even when unimodal waveforms merge into a single envelope due to high-frequency consecutive coughs, the bimodal sensor system can still accurately extract physiological information through cross-validation. Respiratory responses under different physiological states are presented in Fig. 5e. In the resting state, the temperature and humidity signals are highly synchronized (correlation coefficient >0.95), exhibiting stable waveforms with a respiratory rate of approximately 10.6 breaths per minute (bpm). During exercise, the respiratory rate increases to 22.1 bpm. Under this condition, the humidity channel exhibits signal clipping due to limitations in dynamic adsorption-desorption processes. In contrast, the fast response of the temperature channel compensates for this lag, with its rising slope approximately doubling relative to the resting state, thereby preventing misinterpretation as hypoventilation. It should be noted that the response time of 39.83 s, measured under a relatively large humidity step from 58.2% to 90% RH (Fig. 3l), represents the time required for the sensor to approach its steady-state response and should not be interpreted as the minimum temporal resolution for detecting respiratory events. During respiration, transient variations in local humidity can induce detectable capacitance changes well before complete adsorption equilibrium is established, thereby enabling the humidity channel to track periodic breathing cycles. The humidity signals in the physiological demonstrations were acquired directly without additional temporal filtering. At higher respiratory rates, however, the limited adsorption-desorption kinetics of the GO sensing layer may attenuate the signal amplitude and distort the waveform, although individual respiratory cycles remain distinguishable. Under such conditions, the humidity response is interpreted together with the faster temperature channel, allowing the two sensing modalities to provide complementary dynamic information for respiratory monitoring. During deep breathing, the waveforms display pronounced morphological heterogeneity. Specifically, the humidity signal shows a 1–2 s plateau, while the temperature signal exhibits a sharp, mountain-like peak, reflecting the physiological reduction in airflow rate toward the end of exhalation.

Finally, the sensor was mounted on the dorsal hand to monitor epidermal temperature and humidity during exercise (Fig. 5f), enabling capture of the full thermoregulatory process (Fig. 5g). At the onset of exercise (123 s), both skin temperature and humidity decreased slightly by approximately 0.5 ℃ and 1% RH, respectively, which is due to convective cooling. After 201 s of sustained activity (i.e., at 324 s), the increase in core body temperature triggered sweating, leading to a rapid rise in epidermal humidity accompanied by a decrease in temperature. Exercise ceased at 450 s, at which point the temperature had decreased by 1.2 ℃ (to 30.2 ℃), while humidity had increased by 26% (to 83.3% RH) relative to baseline. Following a brief 10 s decline, humidity continued to increase for an additional 50 s due to a “delayed sweating” effect. During this period, epidermal temperature exhibited a dynamic trend, initially increasing (from 29.9 to 30.9 ℃) and subsequently decreasing (to 29.4 ℃). This behavior reflects the dynamic competition between the cessation of convective cooling and the ongoing evaporative cooling of sweat. Eventually, as the sweat evaporated, both signals gradually returned to their baseline

levels. To demonstrate a representative application that specifically benefits from decoupled temperature-humidity sensing, we added a textile-integrated skin-garment microclimate test, as shown in Fig. 6a. In this experiment, the bimodal sensor was attached to the skin beneath one to three layers of fabric, and the temperature and humidity at the skin-garment interface were simultaneously monitored. Three representative fabrics were investigated: 100% polyester, 100% cotton, and a 50/50 polyester-cotton blend. The results show that the interfacial relative humidity generally increased with the number of fabric layers and was also strongly affected by the fabric composition. Specifically, under the three-layer fabric configuration, polyester exhibited the highest interfacial RH of approximately 68.1% (Fig. 6b), followed by the polyester-cotton blend at 65.1% (Fig. 6c), whereas cotton showed the lowest value of 60.2% (Fig. 6d). Meanwhile, the interfacial temperature increased only slightly (Figs. 6b–6d). This behavior can be attributed to the combined effects of heat dissipation, perspiration, moisture absorption, and fabric breathability. As the number of fabric layers increases, heat and moisture dissipation to the surrounding environment becomes more restricted, leading to greater moisture accumulation at the skin-garment interface. In addition, compared with cotton, polyester has lower moisture absorbency and generally poorer moisture-management capability, resulting in greater humidity accumulation with increasing synthetic fiber content. These results highlight the importance of simultaneously resolving temperature and humidity. Without decoupled bimodal measurements, the observed

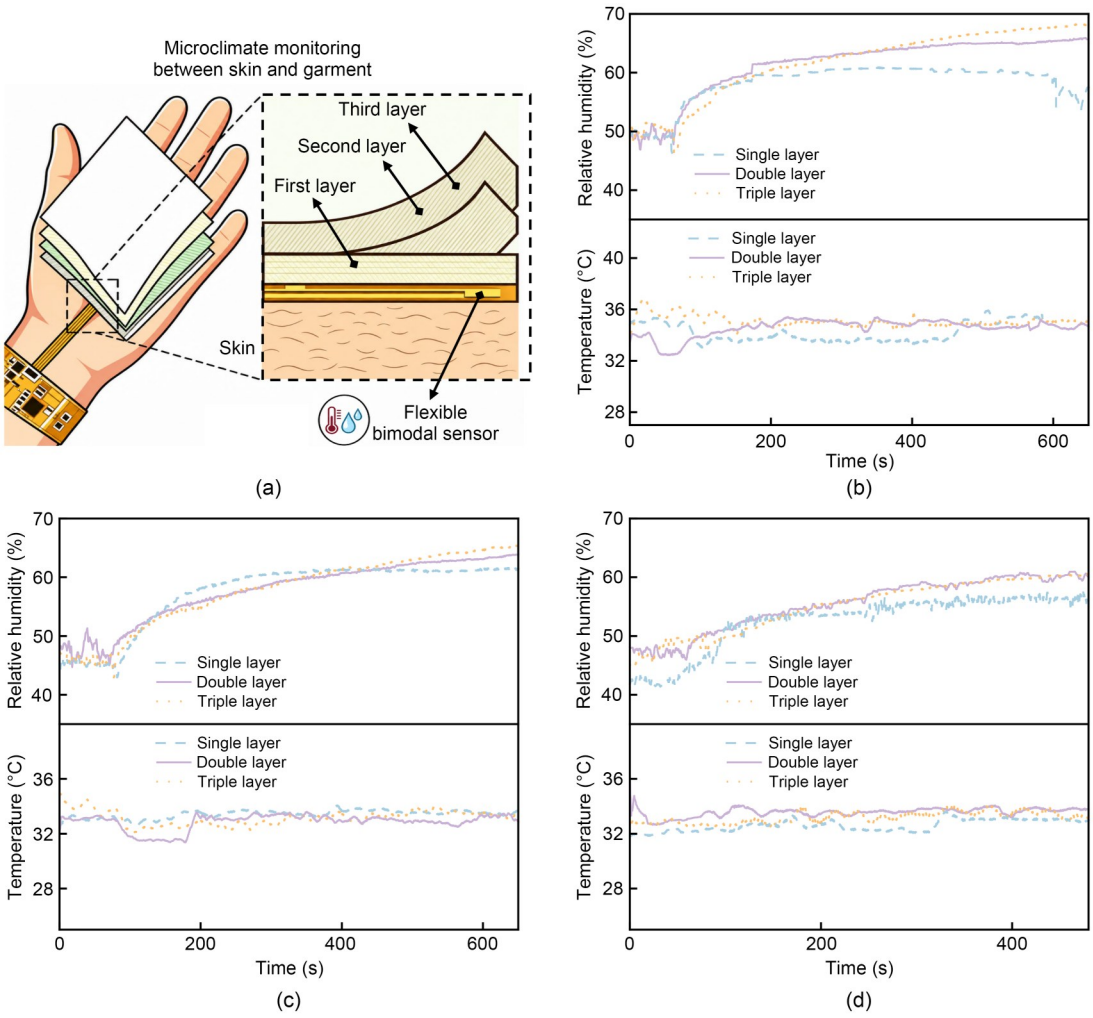

Fig. 6 (a) Schematic illustration of the skin-garment microclimate test configuration with varying fabric layers (single, double, and triple layers); (b–d) simultaneous real-time measurements of relative humidity and temperature at the skin-garment interface for (b) 100% polyester, (c) a 50/50 polyester-cotton blend, and (d) 100% cotton fabrics

microclimate variations could not be reliably distinguished between thermal accumulation and moisture-related effects associated with fabric hygroscopicity and breathability. To place the proposed system in the context of existing flexible temperature-humidity sensors, a comprehensive comparison of sensing performance and system-level characteristics is provided in Table S2 of the ESM.

4 Conclusions

This study presents a flexible epidermal integrated temperature-humidity sensor that suppresses signal crosstalk through the synergistic combination of hybrid ionic-electronic conduction mechanisms and a second-order compensation algorithm. The proposed system effectively addresses the crosstalk issue in multimodal flexible devices during complex physiological monitoring. The heterogeneous integration of copper-constantan thin-film thermocouples allows independent temperature measurements. Meanwhile, UV laser direct writing is employed to fabricate LIG interdigital electrodes in situ on flexible polyimide substrates. Combined with the abundant hydrophilic functional groups of GO, this design enables highly sensitive humidity sensing. Experimental results demonstrate that the integrated sensor achieves a humidity sensitivity of 31 pF/%RH and a temperature sensitivity of 29.88 μV/°C, along with excellent stability under dynamic cyclic operation. A second-order polynomial calibration algorithm reduces humidity measurement error to within 2% RH. Integrated with a self-developed FPC-based sensor readout system, the platform is successfully applied to respiratory monitoring, cough detection, and exercise-induced epidermal temperature-humidity tracking. This synergistic crosstalk suppression strategy offers a viable pathway for the development of multimodal integrated sensors, with broad potential in intelligent healthcare, exercise monitoring, and early detection of respiratory diseases.

Acknowledgments

This work is supported by the National Natural Science Foundation of China (Nos. 52575674, 52325507, and U25A20311).

Author contributions

Mengran LIU and Tao LUO designed the research and contributed to the preparation and revision of the manuscript. Wendi GAO and Tao LUO supervised the research. Ziming LI performed the main experimental work and processed and analyzed the corresponding data. Yingying DAI, Chongjie JIANG, Junwen HUANG, Zhenghong LUO, Jinhui ZHANG, and Wei ZHOU assisted with the experimental work. All authors read and approved the final version of the manuscript.

Conflict of interest

Mengran LIU, Ziming LI, Yingying DAI, Chongjie JIANG, Junwen HUANG, Zhenghong LUO, Jinhui ZHANG, Wei ZHOU, Wendi GAO, and Tao LUO declare that they have no conflict of interest.

Declaration on the use of generative AI tools

During the preparation of this work, the authors used DeepSeek to improve the language and readability of the manuscript. After using this tool, the authors reviewed and edited the content as needed and take full responsibility for the content of the published article.

Data availability

The data that support the findings of this study are available from the corresponding author upon reasonable request.

References

Baker LB, Model JB, Barnes KA, et al., 2020. Skin-interfaced microfluidic system with personalized sweating rate and sweat chloride analytics for sports science applications. *Science Advances*, 6(50):eabe3929. https://doi.org/10.1126/sciadv.abe3929

Bandodkar AJ, Gutruf P, Choi J, et al., 2019. Battery-free, skin-interfaced microfluidic/electronic systems for simultaneous electrochemical, colorimetric, and volumetric analysis of sweat. *Science Advances*, 5(1):eaav3294. https://doi.org/10.1126/sciadv.aav3294

Bi HC, Yin KB, Xie X, et al., 2013. Ultrahigh humidity sensitivity of graphene oxide. *Scientific Reports*, 3(1):2714. https://doi.org/10.1038/srep02714

Choi G, Ko SH, 2026. Laser-induced graphene for micro- and nano-manufacturing: fundamentals, processing approaches, and emerging applications. *Micro & Nano Manufacturing*, 2(1):12. https://doi.org/10.1007/s44374-026-00021-0

Choi G, Yoon S, Jung Y, et al., 2026. Robust freestanding laser-induced graphene electrodes for wearable energy devices. *Carbon*, 246:120852. https://doi.org/10.1016/j.carbon.2025.120852

Fei XX, Huang JY, Shi WQ, 2023. Humidity sensor composed of laser-induced graphene electrode and graphene oxide for monitoring respiration and skin moisture. *Sensors*, 23(15):6784. https://doi.org/10.3390/s23156784

Gao W, Emaminejad S, Nyein HYY, et al., 2016. Fully integrated wearable sensor arrays for multiplexed in situ perspiration analysis. *Nature*, 529(7587):509-514.

https://doi.org/10.1038/nature16521

Ghosh S, Ghosh R, Guha PK, et al., 2015. Humidity sensor based on high proton conductivity of graphene oxide. *IEEE Transactions on Nanotechnology*, 14(5):931-937. https://doi.org/10.1109/tnano.2015.2465859

Jia QS, Ye WH, Zhang C, et al., 2025. Wearable multimodal sensing system for synchronously health–environmental monitoring via hybrid neuroevolutionary signal decoupling. *Nano Letters*, 25(24):9726-9733. https://doi.org/10.1021/acs.nanolett.5c01881

Jung Y, Min J, Choi J, et al., 2022. Smart paper electronics by laser-induced graphene for biodegradable real-time food spoilage monitoring. *Applied Materials Today*, 29:101589. https://doi.org/10.1016/j.apmt.2022.101589

Kim J, Campbell AS, de Ávila BEF, et al., 2019. Wearable biosensors for healthcare monitoring. *Nature Biotechnology*, 37(4):389-406. https://doi.org/10.1038/s41587-019-0045-y

Kim KK, Ha I, Kim M, et al., 2020. A deep-learned skin sensor decoding the epicentral human motions. *Nature Communications*, 11(1):2149. https://doi.org/10.1038/s41467-020-16040-y

Kim KK, Kim M, Pyun K, et al., 2023. A substrate-less nanomesh receptor with meta-learning for rapid hand task recognition. *Nature Electronics*, 6(1):64-75. https://doi.org/10.1038/s41928-022-00888-7

Kim KK, Bang J, Kim M, et al., 2026. Unisensory processing of interleaving memristive nanowires enabling multimodal sensing at human-scale resolution. *Nature Materials*, 25(3):463-471. https://doi.org/10.1038/s41563-025-02373-w

Kuzubasoglu BA, 2022. Recent studies on the humidity sensor: a mini review. *ACS Applied Electronic Materials*, 4(10):4797-4807. https://doi.org/10.1021/acsaelm.2c00721

Lan LY, Le XH, Dong HY, et al., 2020. One-step and large-scale fabrication of flexible and wearable humidity sensor based on laser-induced graphene for real-time tracking of plant transpiration at bio-interface. *Biosensors and Bioelectronics*, 165:112360. https://doi.org/10.1016/j.bios.2020.112360

Le TSD, Phan HP, Kwon S, et al., 2022. Recent advances in laser-induced graphene: mechanism, fabrication, properties, and applications in flexible electronics. *Advanced Functional Materials*, 32(48):2205158. https://doi.org/10.1002/adfm.202205158

Liu DY, Tian XY, Bai J, et al., 2024. A wearable in-sensor computing platform based on stretchable organic electrochemical transistors. *Nature Electronics*, 7(12):1176-1185. https://doi.org/10.1038/s41928-024-01250-9

Mu YB, Cheng JG, Shi W, et al., 2024. Crosstalk-free hybrid integrated multimodal sensor for human temperature, humidity, and pressure monitoring. *Cell Reports Physical Science*, 5(10):102223. https://doi.org/10.1016/j.xcrp.2024.102223

Nyein HYY, Bariya M, Tran B, et al., 2021. A wearable patch for continuous analysis of thermoregulatory sweat at rest. *Nature Communications*, 12(1):1823. https://doi.org/10.1038/s41467-021-22109-z

Park H, Choi G, Yoon S, et al., 2026. Convergence of soft electronics and artificial intelligence: from materials to intelligent systems. *Nano-Micro Letters*, 18(1):419. https://doi.org/10.1007/s40820-026-02265-x

Ren ZH, Shi XY, Yang Q, et al., 2025. An ultrastretchable seamlessly integrated contactless charging microsystem towards skin-attachable wireless microelectronics. *Nature Communications*, 16(1):1642. https://doi.org/10.1038/s41467-025-56881-z

Rohilla R, Prakash J, Dasgupta K, 2025. Review of carbon nanotube/graphene nanosheet chemiresistive gas sensors. *ACS Applied Nano Materials*, 8(49):23414-23465. https://doi.org/10.1021/acsanm.5c04068

Shen S, Zhou Q, Chen GR, et al., 2024. Advances in wearable respiration sensors. *Materials Today*, 72:140-162. https://doi.org/10.1016/j.mattod.2023.12.003

Wu J, Wu ZX, Ding HJ, et al., 2019. Multifunctional and high-sensitive sensor capable of detecting humidity, temperature, and flow stimuli using an integrated microheater. *ACS Applied Materials & Interfaces*, 11(46):43383-43392. https://doi.org/10.1021/acsami.9b16336

Wu T, Li YT, Zhao LY, et al., 2026. Recent progress on flexible multimodal sensors: decoupling strategies, fabrication and applications. *Advanced Materials*, 38(12):e21375. https://doi.org/10.1002/adma.202521375

Yang RX, Zhang WQ, Tiwari N, et al., 2022. Multimodal sensors with decoupled sensing mechanisms. *Advanced Science*, 9(26):2202470. https://doi.org/10.1002/advs.202202470

Yin ZF, Yang Y, Hu C, et al., 2024. Wearable respiratory sensors for health monitoring. *NPG Asia Materials*, 16(1):8. https://doi.org/10.1038/s41427-023-00513-9

Yuan YB, Zhang WQ, Yang JY, et al., 2026. Recent advances in decoupling strategies for soft sensors. *Advanced Science*, 13(17):e14499. https://doi.org/10.1002/advs.202514499

Zhou L, Guess M, Kim KR, et al., 2024. Skin-interfacing wearable biosensors for smart health monitoring of infants and neonates. *Communications Materials*, 5(1):72. https://doi.org/10.1038/s43246-024-00511-6

Zhu CC, Tao LQ, Wang Y, et al., 2020. Graphene oxide humidity sensor with laser-induced graphene porous electrodes. *Sensors and Actuators B: Chemical*, 325:128790. https://doi.org/10.1016/j.snb.2020.128790

Electronic supplementary materials

Figs. S1–S4 and Tables S1 and S2